Journal of Alloys and Compounds 976 (2024) 173044

Contents lists available at ScienceDirect

Journal of Alloys and Compounds

journal homepage: www.elsevier.com/locate/jalcom

Mn^{5+}-doped $BaAl_2O_4$, $Ba_3Al_2O_6$, and $Ba_7Al_2O_{10}$ phosphors emitting in the second near-infrared biological window

Hang Zhao [a], Xin Xin [a], Qiuying Wang [a], Zhiwei Wang [a], Yuqian Wang [a], Qiuyu Cheng [a], Theeranun Siritanon [b], M.A. Subramanian [c], Peng Jiang [a,*]

[a] School of Materials Science and Engineering, University of Science and Technology Beijing, Beijing 100083, China
[b] School of Chemistry, Institute of Science, Suranaree University of Technology, 111 University Avenue, Muang, Nakhon Ratchasima 30000, Thailand
[c] Department of Chemistry, Oregon State University, Corvallis, OR 97330, USA

ARTICLE INFO

Keywords:
Mn^{5+} doping
BaO-Al_2O_3 system
Near-infrared emission
Phosphor

ABSTRACT

In recent years, NIR-II-type fluorophores with emission wavelengths within the 1000–1700 nm range have garnered widespread attention in the field of bioimaging due to their high tissue penetration ability. Here, Mn-doped $BaAl_2O_4$, $Ba_3Al_2O_6$, and $Ba_7Al_2O_{10}$ with NIR-II-type luminescence were synthesized by solid-phase or liquid-phase methods. Confirmed by XPS and EDS analysis, Mn is found uniformly distributed in the structure in the valence state of + 5. The optimal doping concentration of Mn^{5+} in the three matrices was analyzed by PLE and PL spectroscopy. In addition, the samples exhibit a wide excitation range spanning from 600 to 900 nm, coupled with a narrow emission band peaking between 1150 and 1200 nm. As both the excitation and emission wavelengths have excellent penetration capabilities in biological tissues, the synthesized fluorescent phosphors in this study hold potential for meaningful applications in the realm of fluorescence imaging.

1. Introduction

Biological imaging technologies including magnetic resonance imaging, computed X-ray tomography, optical imaging, and fluorescence imaging are of great importance in the biological field [1]. Owing to fast feedback and high sensitivity [2], fluorescence imaging technology has become one of the fastest-growing techniques in the biomedical field [3]. The emission wavelengths of traditional fluorescence imaging technology are located in the first near-infrared biological window (NIR-I, wavelength 700–900 nm) [4]. Two NIR-I fluorescent dyes which shows deeper tissue penetration than visible light, indocyanine green and methylene blue, are already certified in the United States [5]. However, their wavelength shifts are relatively small and they have a certain background noise, which tends to limit their applications. In 2009, scientists at Stanford University revealed a new biological imaging window called the second near-infrared biological window (NIR-II, wavelength 1000–1700 nm) [6]. In contrast to NIR-I, NIR-II has better tissue penetration ability. Furthermore, it reduces photon scattering and background fluorescence, resulting in higher resolution and sensitivity [7]. Consequently, over the past decade or so, researchers have primarily focused on NIR-II. Various systems of NIR-II-type fluorophores have emerged, including single-walled carbon nanotubes (SWCNTs) [8], various quantum dots (QDs) [9], rare-earth doped nanoparticles (RENPs) [10], a few organic dyes [11] and so on. However, these fluorophores also have certain limitations. SWCNTs and QDs exhibit lower fluorescence quantum yields, and certain QDs may potentially present toxicity risks to human health [12]. The rare-earth elements in RENP require higher costs, while organic dyes have poor photostability [13]. These limitations have restricted their further application in the field of biomedical research. So for the time being, scholars continue to explore new fluorophores to overcome the shortcomings of the above fluorophores.

Previous research has revealed that due to the $^1E \rightarrow {}^3A_2$ transition of Mn^{5+}, Mn^{5+}-doped materials emit near-infrared light within the wavelength spectrum of 1000–1300 nm upon excitation [14]. This emission falls precisely within the NIR-II window range. Mn^{5+}-doped materials exhibit higher quantum efficiency than SWCNTs and QDs [15]. Moreover, it has good biocompatibility as it does not contain toxic heavy metals. Compared with rare earth elements, Mn^{5+} has a lower cost and emits a stronger near-infrared signal, showing good photostability. Due to these advantages, Mn^{5+}-doped materials have the potential to become novel NIR-II fluorescent materials. Zhang [16] et al. successfully

* Corresponding author.
E-mail address: jiangp@ustb.edu.cn (P. Jiang).

https://doi.org/10.1016/j.jallcom.2023.173044
Received 21 September 2023; Received in revised form 13 November 2023; Accepted 1 December 2023
Available online 3 December 2023

synthesized $Ba_3(MO_4)_2$:Mn^{5+} (M = V, P) nanoparticles. They injected the fluorescent powder into 5 mm thick pork tissue and used 800 nm light for excitation. The infrared camera was able to clearly observe its emitted light, demonstrating that light in the second near-infrared window has good penetration capability. This also validates the potential application of fluorescent powder in the field of biological imaging. However, Mn^{5+} is not stable and is prone to self-disproportionation in oxides [17]. Therefore, to successfully dope Mn^{5+}, it is necessary to find a suitable matrix that can provide a stable environment for Mn^{5+}.

We found that Mn^{5+} can stably exist in tetrahedral positions in certain silicates and phosphates. For example, Zhang [16] et al. prepared Mn^{5+} doped Ba_2SiO_4 phosphors with Mn^{5+} replacing Si^{4+} in [SiO_4] tetrahedra by solid-phase method. Cao [15]et al. used solid-phase method to synthesize $Ba_3(PO_4)_2$:Mn^{5+} phosphor with Mn^{5+} substituting P^{5+} in [PO_4] tetrahedra. Additionally, the presence of alkaline earth metal ions such as Ba^{2+} and Ca^{2+} also supports the stability of Mn^{5+}. Al_2O_3 is abundant in nature, inexpensive. So Al_2O_3 and $BaCO_3$ as the main raw material for the preparation of phosphor also has a good industrial value. Our previous studies has proved the successful doping of Mn^{5+} in $BaAl_2O_4$, $Ba_3Al_2O_6$ and $Ba_7Al_2O_{10}$ in BaO-Al_2O_3 system, producing intense turquoise colors [18–20]. However, their potential in NIR-II is not evaluated. The structures of $BaAl_2O_4$ and $Ba_3Al_2O_6$ are shown in Fig. 1. $BaAl_2O_4$ belongs to a stuffed tridymite-like structure, and its main structural unit is the angularly connected [AlO_4] tetrahedra. [21] The structure of $Ba_3Al_2O_6$ is a defective chalcogenide structure, and its main structural unit is the 12-membered [AlO_4] ring crosslinked by Ba^{2+} [22]. The structure of $Ba_7Al_2O_{10}$ is unknown. However, FT-IR and Al NMR analyses of the $Ba_7Al_2O_{10}$ structure by our previous study demonstrated that the basic structural units of $Ba_7Al_2O_{10}$ also include [AlO_4] tetrahedra [18]. All three structures include a large number of tetrahedral coordination, which can provide a more stable environment for Mn^{5+}. Currently, there is no report on Mn^{5+}-doped BaO-Al_2O_3 system phosphors, so the work in this paper is to synthesize Mn^{5+}-doped $BaAl_2O_4$, $Ba_3Al_2O_6$, and $Ba_7Al_2O_{10}$ with different contents by solid-phase or liquid-phase methods. Because the solid-state method is simple in procedure and satisfied in production rate, this paper primarily uses the solid-state method. However, $BaAl_{2-x}Mn_xO_{4+x}$ ($x = 0.01$, 0.03, 0.05) samples cannot be prepared using the solid-state method, so the sol-gel method is employed. The luminescent properties of Mn^{5+} in these three matrices will be analyzed through spectroscopic analysis, and their potential applications in fluorescence imaging are explored.

2. Experimental

2.1. Sample preparation

$BaAl_{2-x}Mn_xO_{4+x}$ ($x = 0.01$, 0.03, 0.05) were prepared by sol-gel method. $Al(NO_3)_3{\cdot}9\,H_2O$, and $Mn(C_2H_3O_2)_2{\cdot}4\,H_2O$ were weighed based on the stoichiometric proportions, then combined in a beaker containing 50 ml of deionized water and thoroughly stirred. Citric acid was introduced into the solution at a 3:1 ratio (citric acid to metal ions) and then ultrasonicated for 15 min until a clear solution was obtained. The beaker was placed in a water bath maintained at 70 °C and stirred magnetically until gels were formed. Subsequently, the gels were subjected to a 12 h drying process at 140 °C in an oven and ground to obtain the precursors. The precursors were heated at 600 °C for 1 h to remove carbon. Finally, the samples were heated to 1000 ℃ for 12 h in a box furnace.

$Ba_3Al_{2-x}Mn_xO_{6+x}$ ($x = 0.01$, 0.03, 0.05) were synthesized by high-temperature solid phase method. $BaCO_3$, Al_2O_3, and MnO_2 were weighed based on the stoichiometric proportions and then placed in a ball milling jar at 300 r/min for 600 min. Then, 2/3 vol of ethanol was added and wet milled for 30 min. The well-mixed raw materials were poured into a beaker and dried in a 50 ℃ oven for 12 h. After drying, the materials were ground, pressed, and placed in corundum crucibles. Finally, the samples were heated to 1300 ℃ for 12 h in a box furnace. This sintering process was repeated twice to obtain the samples.

$Ba_7Al_{2-x}Mn_xO_{10+x}$ ($x = 0.01$, 0.03, 0.05) were prepared by high-temperature solid phase method. $BaCO_3$, Al_2O_3, and MnO_2 were weighed based on the stoichiometric proportions and placed into a mortar. Then they were ground for 20 min to ensure uniform mixing. The mixed raw materials were compressed into pellets and introduced into corundum crucibles. Finally, the samples were heated to 1200 ℃ for 12 h in a box furnace.

2.2. Characterization

The X-ray diffraction (XRD) patterns were acquired using a Bruker D8 Advance diffractometer, employing Ni-filtered Cu Kα (λ = 0.15415 nm) radiation. The data were gathered over a 2θ range spanning from 15° to 65°, with a scanning rate of 10°/min. Sample morphologies were observed by a field emission scanning electron microscope (FESEM, GeminiSEM 500), and the chemical compositions were tested using energy dispersive spectroscopy (EDS, Oxford X-Max). The binding energy was acquired using X-ray photoelectron spectroscopy (XPS, ESCALAB 250XI). The excitation source used was Al Kα-rays (1486.6 eV), and the full-spectrum scan was performed at a fluence energy of 150 eV with a step of 1 eV; the narrow-spectrum scan was performed at a fluence energy of 50 eV with a step of 0.1 eV. The fluorescence spectrophotometer (Edinburgh Instruments, FLS1000) equipped with a continuous 500 W xenon lamp was utilized to acquire the photoluminescence (PL) spectra, photoluminescence excitation (PLE) spectra, and fluorescence decay curves.

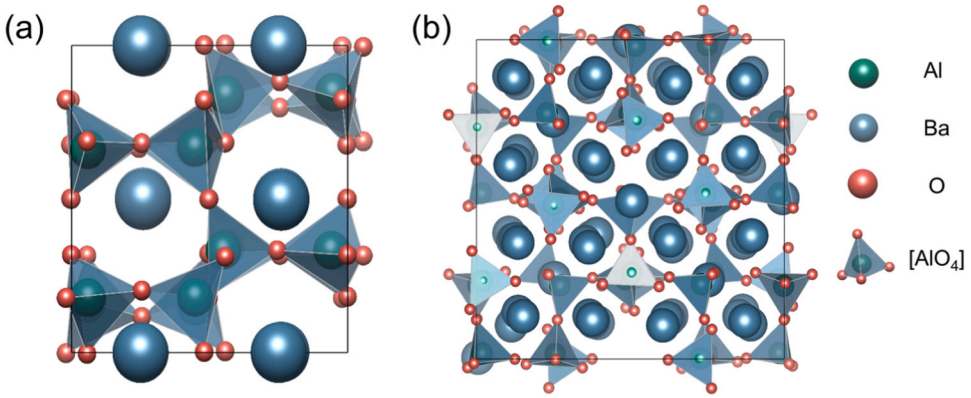

Fig. 1. Crystal structures of (a)$BaAl_2O_4$, (b)$Ba_3Al_2O_6$.

3. Results and discussion

3.1. X-ray diffraction analysis

Fig. 2(a) and Fig. 2(b) show the XRD patterns of $BaAl_{2-x}Mn_xO_{4+x}$ ($x = 0.01, 0.03, 0.05$) and $Ba_3Al_{2-x}Mn_xO_{6+x}$ ($x = 0.01, 0.03, 0.05$) samples. The diffraction peaks of $BaAl_{2-x}Mn_xO_{4+x}$ ($x = 0.01, 0.03, 0.05$) and $Ba_3Al_{2-x}Mn_xO_{6+x}$ ($x = 0.01, 0.03, 0.05$) samples correspond well to the standard $BaAl_2O_4$ (PDF#72–0387) pattern and standard $Ba_3Al_2O_6$ (PDF#25–0075) pattern, and no other impurity phases are observed. The peak positions remain constant with increasing Mn doping content, which suggests that low amounts of Mn doping have little effect on the crystal structure.Fig. 2(c) shows X-ray diffraction patterns of $Ba_7Al_{2-x}Mn_xO_{10+x}$ ($x = 0.01, 0.03, 0.05$) samples. The diffraction peaks of $Ba_7Al_{2-x}Mn_xO_{10+x}$ ($x = 0.01, 0.03, 0.05$) samples can be indexed to the standard $Ba_7Al_2O_{10}$ (PDF#41–0164) pattern. When $x = 0.01$, background noise and small unknown impurity peaks can be observed. However, as the doping amount of Mn increases, the background noise and other impurity peaks gradually decrease. This is because the appropriate doping of Mn has a positive impact on improving the stability of $Ba_7Al_2O_{10}$ [18]. Since the intensities of the impurity peaks are very weak for all three samples, their effect on the optical properties is negligible.

In order to further explore the crystal structure changes after Mn doping, $BaAl_{1.99}Mn_{0.01}O_{4.01}$ and $Ba_3Al_{1.99}Mn_{0.01}O_{6.01}$ samples were selected as representatives for Rietveld refinement. The data obtained from the refinement are listed in Table 1 and Fig. 3. It can be seen that the Rp, Rwp, Rexp and GOF values for both samples are within the permissible range, indicating the accuracy of the refinement results and again demonstrating the purity of the samples.

3.2. XPS analysis

To determine the valence state of Mn-doped into the three structures, XPS tests were performed on the samples of $BaAl_{1.95}Mn_{0.05}O_{4.05}$, $Ba_3Al_{1.95}Mn_{0.05}O_{6.05}$, and $Ba_7Al_{1.95}Mn_{0.05}O_{10.05}$. The obtained binding energy full scan and detailed profile analysis of Mn 2p are shown in Fig. 4. From the Fig. 4, the signals of Ba, O, and Al elements can be clearly observed, but due to the low doping concentration of Mn, the peak position of Mn needs to be amplified for observation. The binding energies of Mn at the peak positions of $BaAl_{1.95}Mn_{0.05}O_{4.05}$, $Ba_3Al_{1.95}Mn_{0.05}O_{6.05}$, and $Ba_7Al_{1.95}Mn_{0.05}O_{10.05}$ samples are obtained from the fitting as 642.4 eV, 642.6 eV, and 642.3 eV, respectively. Since the highest Mn doping concentration we used was 0.05% for $Ba_7Al_{1.95}Mn_{0.05}O_{10.05}$, the Mn proportion is very small, resulting in a large error in the test. In our previous study on samples with high concentration of Mn-doped $Ba_7Al_2O_{10}$, the binding energy of Mn was tested to be 642.4 eV [18]. From previous studies, it was observed that as the valence state of Mn increases, its binding energy also exhibits a corresponding increase. Among them, the binding energies of Mn 2p 3/2 in MnO_2 (Mn^{4+}) and K_2MnO_4 (Mn^{6+}) are 641.9 eV and 643.8 eV [23]. Hence, it is inferred that the binding energies of Mn^{5+} in the oxides are roughly in the range of 641.9–643.8 eV. The binding energies of Mn^{5+} in $Ba_2In_{2-x}Mn_xO_5$ and $Ca_6Ba(P_{1-x}Mn_x)_4O_{17}$ are 642.75 eV [24] and 642.80 eV [25], which are close to the binding energies of the three as-synthesized samples. This allows us to make an initial assessment that the chemical valence of Mn is + 5. Since Mn is doped to [AlO_4] in the form of Mn^{5+}, with no influence on Ba^{2+} content. Therefore, it is necessary to introduce O^{2-} to balance the charge. Since Mn^{5+} is in place of Al^{3+}, the introduction of x content of Mn^{5+} requires the introduction of x content of O^{2-} to balance the charge. So the structural formulae of the three substrates in this paper are $Ba_3Al_{2-x}Mn_xO_{6+x}$, $BaAl_{2-x}Mn_xO_{4+x}$, and $Ba_7Al_{2-x}Mn_xO_{10+x}$.

Table 1
Summary of Rietveld refinement results of $BaAl_{1.99}Mn_{0.01}O_{4.01}$ and $Ba_3Al_{1.99}Mn_{0.01}O_{6.01}$.

samples	$BaAl_{1.99}Mn_{0.01}O_{4.01}$	$Ba_3Al_{1.99}Mn_{0.01}O_{6.01}$
Space group	P63	P213
Rwp(%)	8.49	8.67
Rp(%)	5.96	6.42
Rexp(%)	5.56	6.21
GOF	1.53	1.40
a(Å)	16.51	10.44
c(Å)	16.51	8.78
V(Å^3)	4506.56	830.12

3.3. Microstructure analysis

Fig. 5(a), Fig. 5(c), and Fig. 5(e) show SEM images of $BaAl_{1.95}Mn_{0.05}O_{4.05}$, $Ba_3Al_{1.95}Mn_{0.05}O_{6.05}$, and $Ba_7Al_{1.95}Mn_{0.05}O_{10.05}$ samples. It can be seen that $Ba_3Al_{1.95}Mn_{0.05}O_{6.05}$ and $Ba_7Al_{1.95}Mn_{0.05}O_{10.05}$ prepared by the solid-phase method are composed of irregular particles, with some small particles adhering on top of the large particles. This is a typical morphology of solid-state synthesized products, and the particle diameters are mainly distributed in the range of 2–10 μm. $BaAl_{1.95}Mn_{0.05}O_{4.05}$ prepared through the liquid-phase method has a similar overall morphology to the previous two samples, with particle diameters also around 2–10 μm. This is likely due to the agglomeration of particles caused by longer sintering time. Fig. 5(b), Fig. 5(d), and Fig. 5(f) show EDS and elemental mapping images of $BaAl_{1.95}Mn_{0.05}O_{4.05}$, $Ba_3Al_{1.95}Mn_{0.05}O_{6.05}$, and $Ba_7Al_{1.95}Mn_{0.05}O_{10.05}$ samples. It can be seen that the signal of Mn is relatively weak due to the low doping level of Mn. However, Mn is still uniformly distributed on the particles. In addition, EDS measurements provide a depth of approximately 1 μm and giving semi-quantitative information about the elemental composition, so the

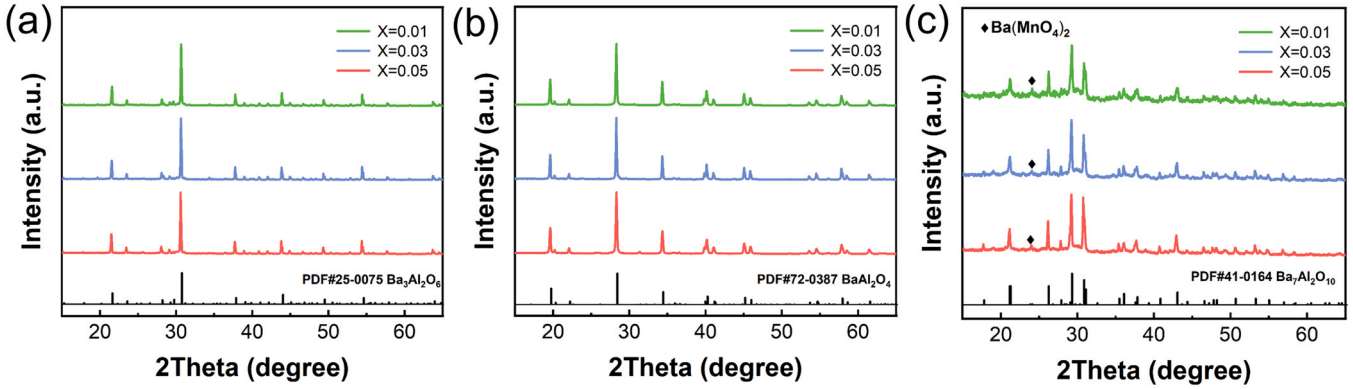

Fig. 2. X-ray diffraction patterns of (a) $BaAl_{2-x}Mn_xO_{4+x}$ ($x = 0.01, 0.03, 0.05$), (b)$Ba_3Al_{2-x}Mn_xO_{6+x}$ ($x = 0.01, 0.03, 0.05$), (c) $Ba_7Al_{2-x}Mn_xO_{10+x}$ ($x = 0.01, 0.03, 0.05$).

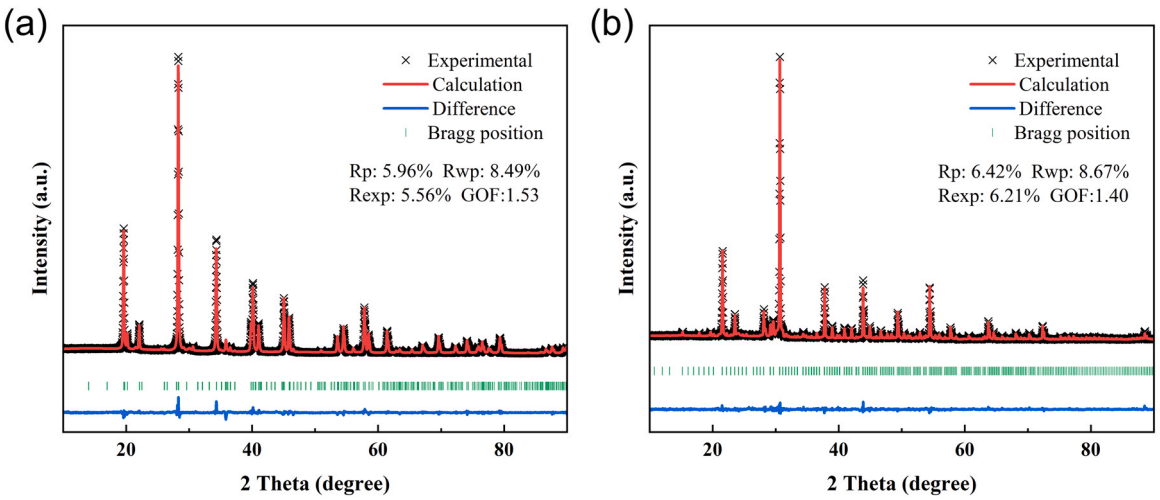

Fig. 3. Rietveld refinement of (a)$BaAl_{1.99}Mn_{0.01}O_{4.01}$,(b)$Ba_3Al_{1.99}Mn_{0.01}O_{6.01}$.

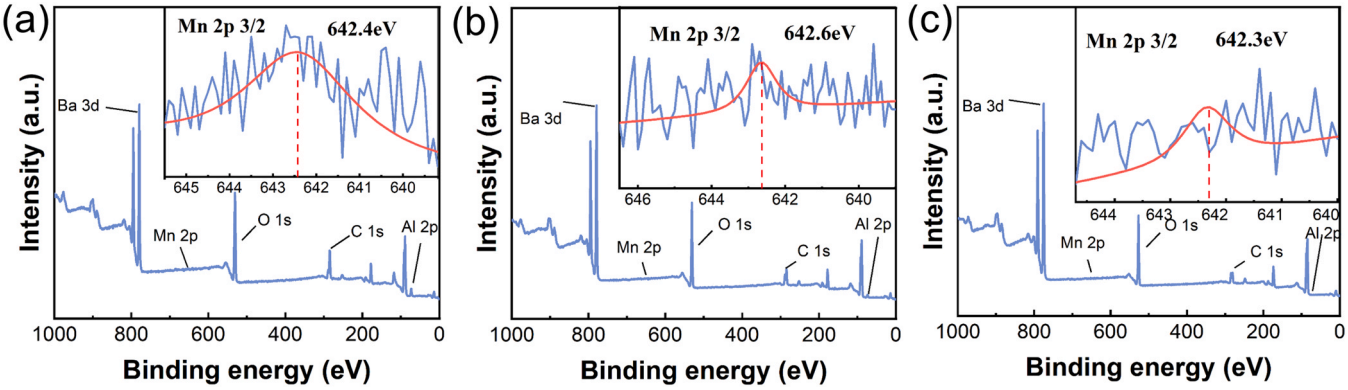

Fig. 4. X-ray photoelectron spectrum of (a)$BaAl_{1.95}Mn_{0.05}O_{4.05}$ ($x = 0.01, 0.03, 0.05$),(b)$Ba_3Al_{1.95}Mn_{0.05}O_{6.05}$ ($x = 0.01, 0.03, 0.05$), (c)$Ba_7Al_{1.95}Mn_{0.05}O_{10.05}$ ($x = 0.01, 0.03, 0.05$).

molar ratios of the measured elements have some errors with the theoretical values [26]. Combined with XRD analysis, it can be preliminarily concluded that Mn^{5+} has been successfully incorporated into the matrix.

3.4. Optical properties

Fig. 6 presents the PLE and PL spectra of $BaAl_{2-x}Mn_xO_{4+x}$ ($x = 0.01, 0.03, 0.05$), $Ba_3Al_{2-x}Mn_xO_{6+x}$ ($x = 0.01, 0.03, 0.05$), and $Ba_7Al_{2-x}Mn_xO_{10+x}$ ($x = 0.01, 0.03, 0.05$) at room temperature. The PLE spectra were obtained under the monitoring of the emission wavelength of 1190 nm. Overall, it was observed that the PLE images of the three groups of samples were similar, indicating that Mn^{5+} are in similar $[AlO_4]$ environments. Additionally, all the samples show a narrow excitation band within the 300–400 nm range, which can be ascribed to the $O^{2-}\rightarrow Mn^{5+}$ charge transfer band (CTB) [27]. There is a broad excitation band between 600 nm and 900 nm, resulted from the transitions of Mn^{5+} including two spin-forbidden transitions $^3A_2\rightarrow{}^3T_1$ and $^3A_2\rightarrow{}^3T_2$, as well as a spin-allowed transition $^3A_2\rightarrow{}^1A_1$ [28]. The excitation wavelengths within the 600–900 nm range correspond well to the first near-infrared window(NIR-I), indicating good tissue penetration capabilities. Furthermore, the PLE spectra of individual samples reveal that the Mn^{5+} concentration influences the signal intensity of the PLE spectra. Fig. 6(a) presents the PLE spectra of $BaAl_{2-x}Mn_xO_{4+x}$ ($x = 0.01, 0.03, 0.05$). As the Mn^{5+} concentration increases, the spectral signal initially increases and then decreases, resulting in a concentration quenching phenomenon. This is because when the Mn^{5+} content increases, the space between Mn^{5+} decreases and their lattice relaxations cross each other thus leading to loss of energy for the jump between energy levels. In addition, as the concentration of the activator ions increases, the probability of energy transfer to impurities or defects in the host matrix and subsequent quenching also increases, resulting in a decrease in luminescence intensity [29]. Therefore, near $x = 0.03$ is the optimal doping concentration for $BaAl_{2-x}Mn_xO_{4+x}$ ($x = 0.01, 0.03, 0.05$). Fig. 6(b) shows that for $Ba_3Al_{2-x}Mn_xO_{6+x}$ ($x = 0.01, 0.03, 0.05$), the Mn^{5+} concentration significantly affects the signal. The signal is strongest at $x = 0.01$, and with the increase in the amount of Mn^{5+} doped, the signal intensity decreases significantly, with $x = 0.01$ being the optimal doping concentration for $Ba_3Al_{2-x}Mn_xO_{6+x}$ ($x = 0.01, 0.03, 0.05$). Fig. 6(c) shows that the variation of Mn^{5+} concentration has little effect on the spectral signal of $Ba_7Al_{2-x}Mn_xO_{10+x}$ ($x = 0.01, 0.03, 0.05$). The signal intensity is slightly higher at $x = 0.05$.

The PL spectra of the samples were obtained using 690 nm excitation light. It is observed that all samples exhibit a sharp emission band within the 1150–1200 nm range, which corresponds to the $^1E\rightarrow{}^3A_2$ spin-forbidden transition of Mn^{5+}. Additionally, there are vibrational bands around 1250 nm ($v_2(e)$) and 1300 nm ($v_1(a_1)$), which correspond to electronic vibrational transitions in MnO_4^{3-} in two different modes [30]. When the excitation signal is stronger, the emission signal also becomes stronger. Fig. 6(d) and Fig. 6(f) show that changes in Mn^{5+} concentration have little effect on the emission peak position of $BaAl_{2-x}Mn_xO_{4+x}$ ($x = 0.01, 0.03, 0.05$) and $Ba_7Al_{2-x}Mn_xO_{10+x}$ ($x = 0.01, 0.03, 0.05$). This suggests that the crystal field environment of these two matrices is hardly affected by variations in Mn^{5+} concentration. In Fig. 6(e), it is evident that as the concentration of Mn^{5+} increases, the emission peak of

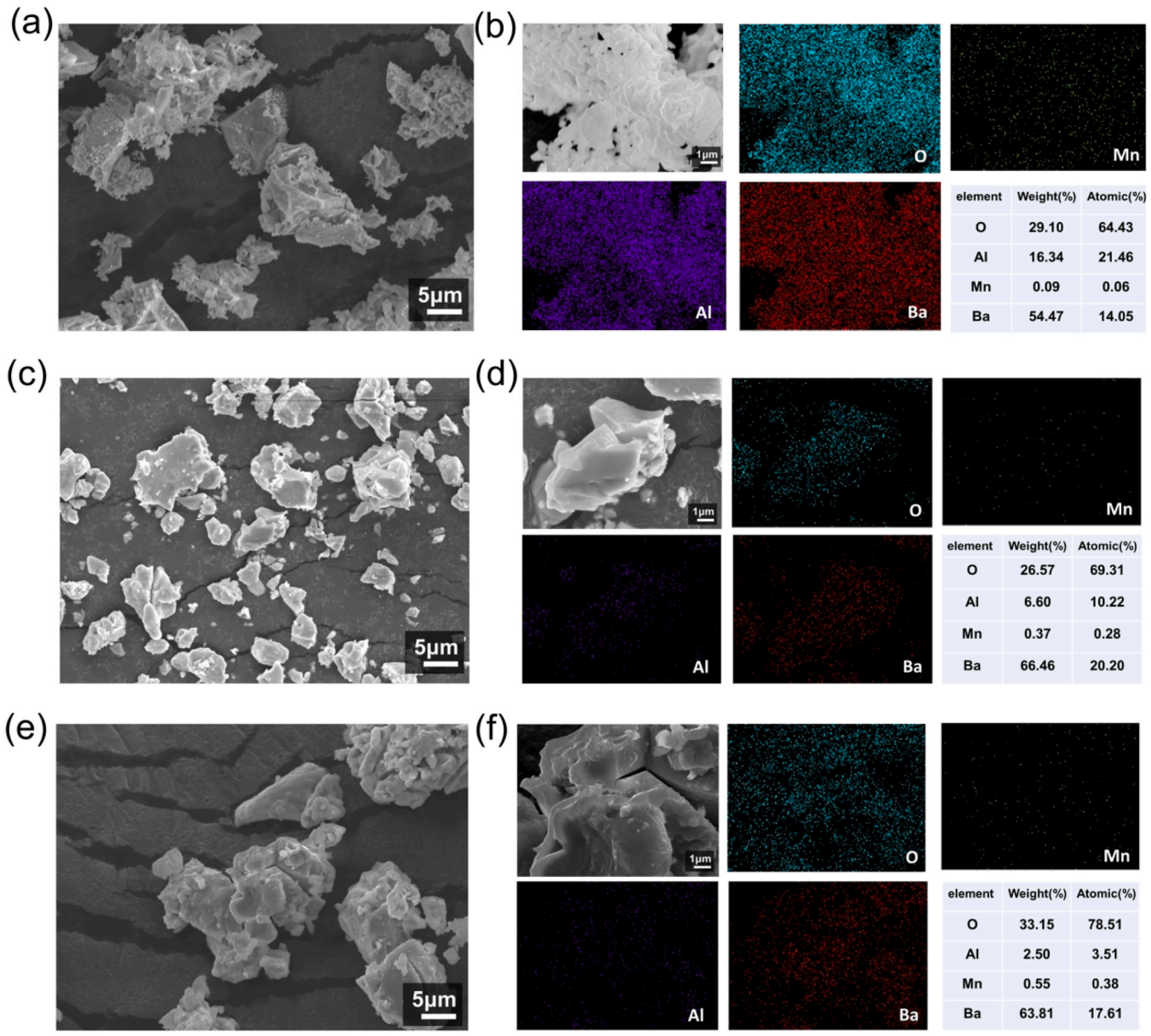

Fig. 5. SEM images of (a)$BaAl_{1.95}Mn_{0.05}O_{4.05}$, (c)$Ba_3Al_{1.95}Mn_{0.05}O_{6.05}$, (e)$Ba_7Al_{1.95}Mn_{0.05}O_{10.05}$; EDS and elemental mapping images of (b)$BaAl_{1.95}Mn_{0.05}O_{4.05}$, (d) $Ba_3Al_{1.95}Mn_{0.05}O_{6.05}$, (f)$Ba_7Al_{1.95}Mn_{0.05}O_{10.05}$.

$Ba_3Al_{2-x}Mn_xO_{6+x}$ ($x = 0.01$, 0.03, 0.05) shifts from 1166 nm to 1194 nm. This shift might be due to an increase in Mn^{5+} concentration leading to a weakening of the crystal field strength. Lastly, it is noteworthy that the emission band of the sample at 1150–1200 nm is located within the second near-infrared window(NIR-II), which is consistent with the luminescence properties of the current NIR-II-type fluorophores.

The outer electron configuration of Mn^{5+} is $3d^2$ When Mn^{5+} is in a tetrahedral coordination, its Tanabe-Sugano energy level diagram is shown in Fig. 7(a). It can be seen that the ^3F ground state splits into three energy levels, $^3A_2$, $^3T_2$ and $^3T_1$, with the $^3A_2$ energy level being the ground state [27]. For Mn^{5+}, the energy of ^1E energy level is lower than $^3T_2$, so ^1E energy level becomes the first excited state. In addition, the slope between the ^1E and the $^3A_2$ energy level curve is very small, so the near-infrared emission range is not easily affected by the crystal field strength [31]. The luminescence process of Mn^{5+} can be illustrated through the simple configuration coordinate diagram of the ion in Fig. 7 (b). After Mn^{5+} is excited by the light of 690 nm, the excited electrons jump from the ground s tate $^3A_2$ to the $^3T_2$, $^1A_1$, and $^3T_1$ levels Subsequently, the excited electron relaxes to the lower-energy ^1E level [32]. Finally, the excited electrons radiatively migrate back to the $^3A_2$ ground state, resulting in near-infrared emission. It can be seen that the luminescence process is basically consistent with the PL and PLE spectra obtained from the tests, so it can be verified again that what we doped is Mn^{5+}.

Fig. 8 shows the luminescence decay curves of $BaAl_{1.99}Mn_{0.01}O_{4.01}$, $Ba_3Al_{1.99}Mn_{0.01}O_{6.01}$, and $Ba_7Al_{1.99}Mn_{0.01}O_{10.01}$ samples under excitation at 690 nm, with monitoring at 1190 nm. The blue points are the experimental data obtained from the measurements and the red curve represents a fitting of the original experimental data. The luminescence decay curves of all three samples were found to fit well to the third-order exponential equation by fitting (R^2 of 0.990, 0.981, and 0.993, respectively). The fitted equations are as follows.

$$I_{(t)}=I_0+A_1e^{-t/\tau1}+A_2e^{-t/\tau2}+A_3^{-t/\tau3}$$

Where $I_{(t)}$ represents the luminescence intensity at time t, I_0 stands for

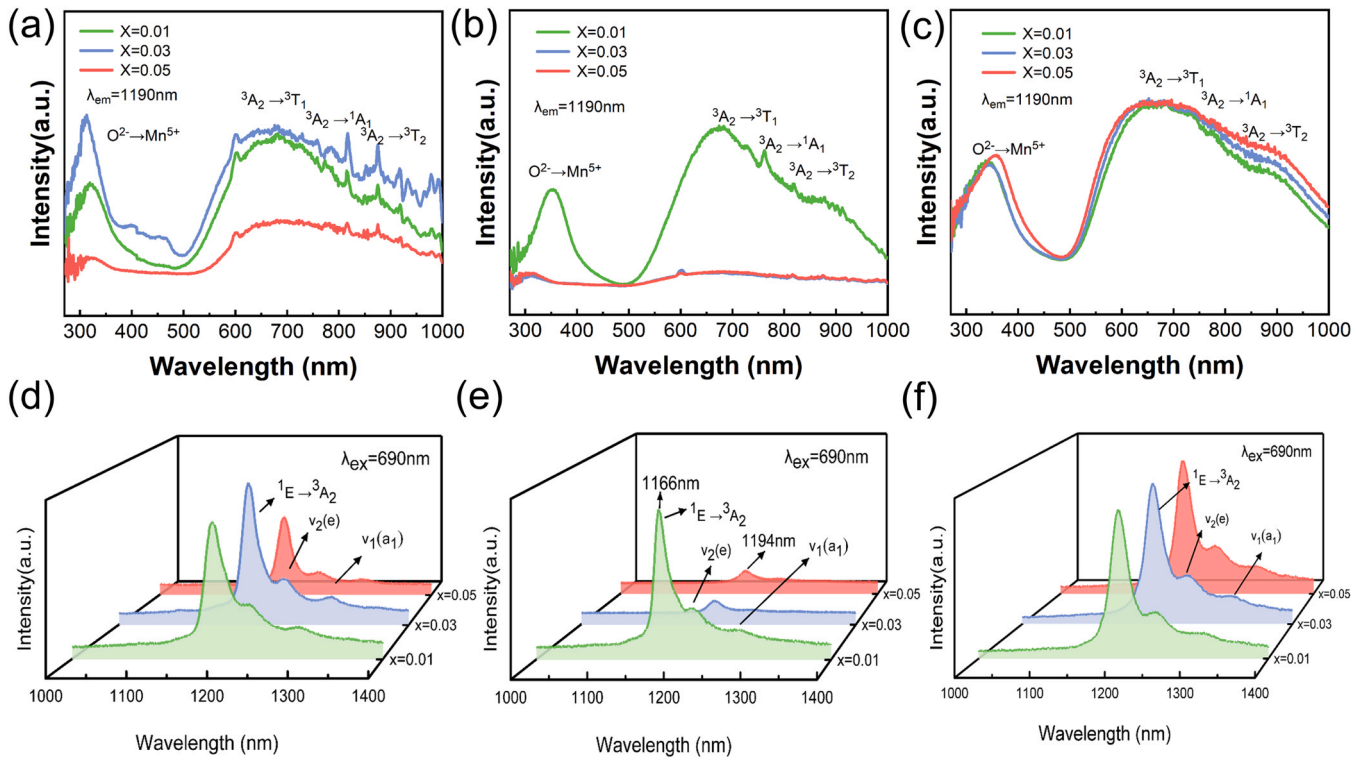

Fig. 6. PLE spectra of (a) $BaAl_{2-x}Mn_xO_{4+x}$ ($x = 0.01, 0.03, 0.05$), (b)$Ba_3Al_{2-x}Mn_xO_{6+x}$ ($x = 0.01, 0.03, 0.05$), (c)$Ba_7Al_{2-x}Mn_xO_{10+x}$ ($x = 0.01, 0.03, 0.05$); PL spectra of (d)$BaAl_{2-x}Mn_xO_{4+x}$ ($x = 0.01, 0.03, 0.05$), (e)$Ba_3Al_{2-x}Mn_xO_{6+x}$ ($x = 0.01, 0.03, 0.05$), (f)$Ba_7Al_{2-x}Mn_xO_{10+x}$ ($x = 0.01, 0.03, 0.05$).

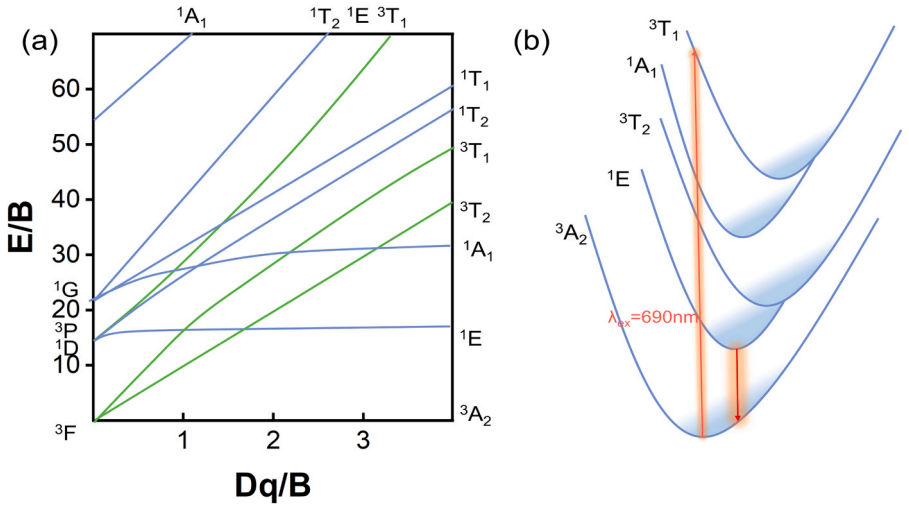

Fig. 7. (a)Tanabe-Sugano energy diagram for Mn^{5+} in tetrahedral coordination; (b)Simple conformational coordinate diagram of the Mn^{5+}.

background or detector zero offset, t represents time, A_1, A_2, and A_3 are constant values, and τ_1, τ_2, τ_3 represent the decay times associated with the exponential components. The average lifetime τ can be computed using the following equation:

$$\tau=(A_1\tau_1^2+A_2\tau_2^2+A_3\tau_3^2)/(A_1\tau_1+A_2\tau_2+A_3\tau_3)$$

The luminescence lifetimes of $BaAl_{1.99}Mn_{0.01}O_{4.01}$, $Ba_3Al_{1.99}Mn_{0.01}O_{6.01}$, and $Ba_7Al_{1.99}Mn_{0.01}O_{10.01}$ samples are finally calculated to be 82.61 μs, 67.99 μs, and 104.50 μs, respectively. The fluorescence lifetimes of traditional NIR-II-type fluorophores are mostly in the nanosecond range. Due to their short lifetimes, there is a possibility of signal confusion with background signals, which can affect imaging accuracy [33]. The sample prepared in this paper has a luminescence lifetime of microseconds, which can allow time-delayed imaging to avoid autofluorescence and thus improve imaging accuracy.

Considering the application of phosphors at different temperatures, we analyzed their thermal stability by conducting PL spectra tests under a continuously changing temperature environment. Fig. 9 shows the emission spectra of $BaAl_{1.99}Mn_{0.01}O_{4.01}$, $Ba_3Al_{1.99}Mn_{0.01}O_{6.01}$, and $Ba_7Al_{1.99}Mn_{0.01}O_{10.01}$ samples within the temperature range of 273–423 K. It is evident that the relationship between temperature and emission intensity is consistent for each sample. As the temperature increases, the shape of the emission peak remains largely unchanged, but the intensity gradually decreases. Both $Ba_3Al_{1.99}Mn_{0.01}O_{6.01}$ and $Ba_7Al_{1.99}Mn_{0.01}O_{10.01}$ samples exhibit a significant drop in emission intensity near 363 K, indicating the occurrence of thermal quenching.

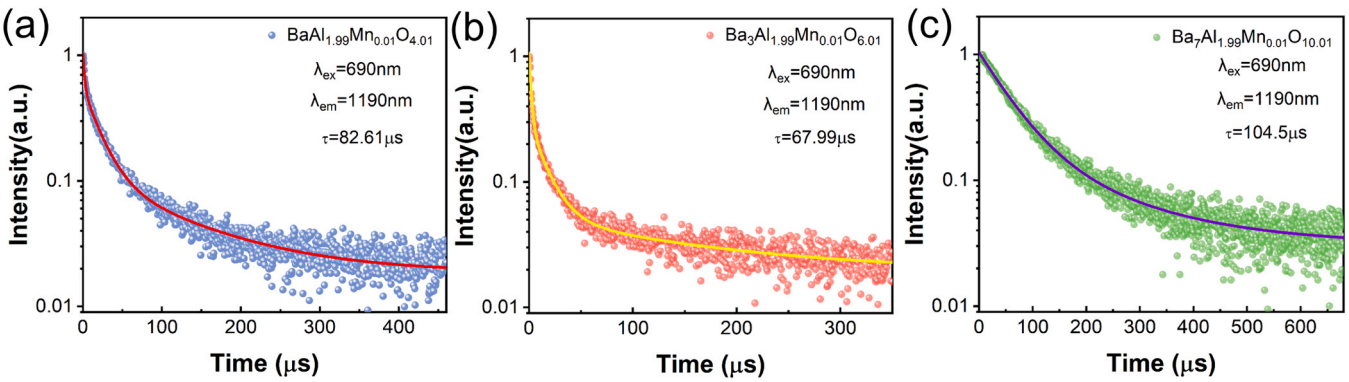

Fig. 8. Luminescence decay curves of (a)$BaAl_{1.99}Mn_{0.01}O_{4.01}$,(b)$Ba_3Al_{1.99}Mn_{0.01}O_{6.01}$, (c)$Ba_7Al_{1.99}Mn_{0.01}O_{10.01}$.

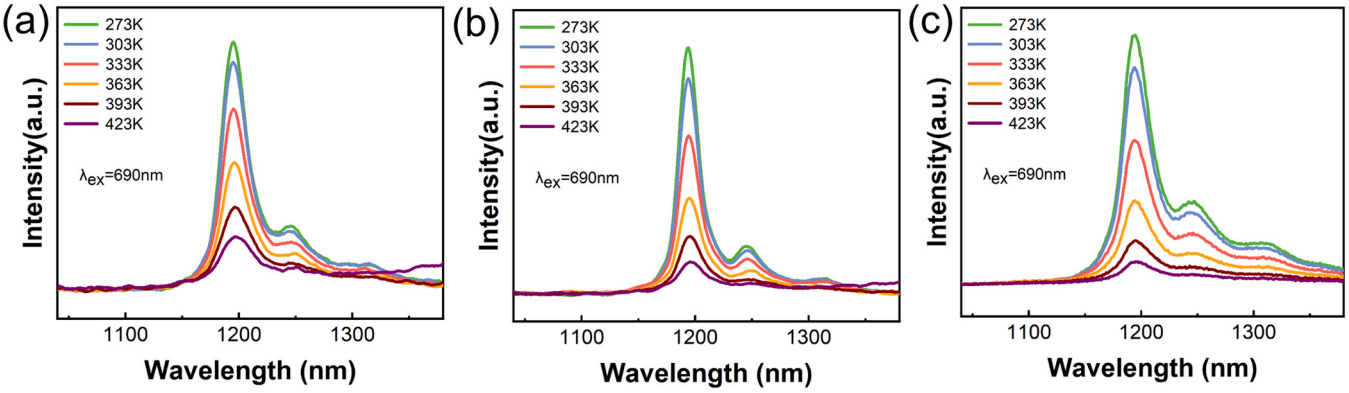

Fig. 9. PL spectra of (a)$BaAl_{1.99}Mn_{0.01}O_{4.01}$, (b)$Ba_3Al_{1.99}Mn_{0.01}O_{6.01}$,(c)$Ba_7Al_{1.99}Mn_{0.01}O_{10.01}$ at different temperatures.

While the $BaAl_{1.99}Mn_{0.01}O_{4.01}$ sample experiences a rapid decrease near 393 K. Compared to the other two samples, it demonstrates better thermal stability. However, considering their potential use in the field of biological fluorescence imaging, all three samples maintain good luminescence intensity within the physiological temperature range.

4. Conclusions

In summary, Mn^{5+}-doped $BaAl_2O_4$, $Ba_3Al_2O_6$, and $Ba_7Al_2O_{10}$ phosphors were successfully synthesized by solid-phase or liquid-phase methods. The optimal doping concentrations for $BaAl_{2-x}Mn_xO_{4+x}$ ($x = 0.01$, 0.03, 0.05), $Ba_3Al_{2-x}Mn_xO_{6+x}$ ($x = 0.01$, 0.03, 0.05), and $Ba_7Al_{2-x}Mn_xO_{10+x}$ ($x = 0.01$, 0.03, 0.05) were determined as $x = 0.03$, $x = 0.01$, and $x = 0.05$, respectively. From the PLE and PL spectra, it can be seen that all the phosphors were excited in the range of 600–900 nm and emitted near-infrared light at 1150–1200 nm. The excitation and emission wavelengths are within the first and second near-infrared biological windows, enabling deeper tissue penetration. Furthermore, the phosphors exhibited luminescence lifetimes in the microsecond range, which is more favorable to the accuracy of imaging. Moreover, all three samples exhibit good luminescent performance within the physiological temperature range. Therefore, these phosphors have potential applications in the field of vivo fluorescence imaging.

CRediT authorship contribution statement

Hang Zhao: Conceptualization, Methodology, Writing – original draft. **Xin Xin:** Data curation, Methodology,Validation. **Qiuying Wang:** Methodology, Investigation. **Zhiwei Wang:** Investigation, Software. **Yuqian Wang:** Investigation. **Qiuyu Cheng:** Investigation, Writing – original draft. **Theeranun Siritanon:** Supervision. **M.A. Subramanian:** Supervision. **Peng Jiang:** Resources , Writing – original draft , Supervision.

Declaration of Competing Interest

The authors declare that they have no known competing financial interests or personal relationships that could have appeared to influence the work reported in this paper.

Data availability

Data will be made available on request.

Acknowledgements

This work was sponsored by Beijing Nova Program under the grant number of 20230484282, the Fundamental Research Funds for the Central Universities under the grant number of FRF-IDRY-22-011, and Youth Teacher International Exchange & Growth Program under the grant No. QNXM20220018. The work done at Oregon State University is supported by US National Science Foundation Grant No. DMR-2025615.

References

[1] Y. Jiang, K. Pu, Molecular probes for autofluorescence-free optical imaging, Chem. Rev. 121 (2021) 13086–13131.
[2] Y. Liu, Q. Jia, J. Zhou, Recent advance in near-infrared (NIR) imaging probes for cancer theranostics, Adv. Ther. 1 (2018).
[3] R. Wang, F. Zhang, NIR luminescent nanomaterials for biomedical imaging, J. Mater. Chem. B 2 (2014) 2422–2443.
[4] W.T. Huang, V. Rajendran, M.H. Chan, M. Hsiao, H. Chang, R.S. Liu, Near-infrared windows I and II phosphors for theranostic applications: spectroscopy, bioimaging, and light-emitting diode photobiomodulation, Adv. Opt. Mater. (11 () (2022).
[5] L. van Manen, H.J.M. Handgraaf, M. Diana, J. Dijkstra, T. Ishizawa, A. L. Vahrmeijer, J.S.D. Mieog, A practical guide for the use of indocyanine green and

methylene blue in fluorescence-guided abdominal surgery, J. Surg. Oncol. 118 (2018) 283–300.
[6] C. Li, G. Chen, Y. Zhang, F. Wu, Q. Wang, Advanced fluorescence imaging technology in the near-infrared-II window for biomedical applications, J. Am. Chem. Soc. 142 (2020) 14789–14804.
[7] G. Hong, J.T. Robinson, Y. Zhang, S. Diao, A.L. Antaris, Q. Wang, H. Dai, In vivo fluorescence imaging with Ag_2S quantum dots in the second near-infrared region, Angew. Chem. Int. Ed. Engl. 51 (2012) 9818–9821.
[8] Z. Liu, S. Tabakman, K. Welsher, H. Dai, Carbon nanotubes in biology and medicine: in vitro and in vivo detection, imaging and drug delivery, Nano Res. 2 (2009) 85–120.
[9] P. Jiang, Z.-Q. Tian, C.-N. Zhu, Z.-L. Zhang, D.-W. Pang, Emission-tunable near-infrared Ag_2S quantum dots, Chem. Mater. 24 (2011) 3–5.
[10] J.C. Zhou, Z.L. Yang, W. Dong, R.J. Tang, L.D. Sun, C.H. Yan, Bioimaging and toxicity assessments of near-infrared upconversion luminescent $NaYF_4$:Yb,Tm nanocrystals, Biomaterials 32 (2011) 9059–9067.
[11] X. Tan, S. Luo, D. Wang, Y. Su, T. Cheng, C. Shi, A. NIR, heptamethine dye with intrinsic cancer targeting, imaging and photosensitizing properties, Biomaterials 33 (2012) 2230–2239.
[12] B.X. Yaping Du, Tao Fu, Miao Cai, Feng Li, Yan Zhang, Qiangbin Wang*, Near-infrared photoluminescent Ag_2S quantum dots from a single source precursor, J. Am. Chem. Soc. 132 (5) (2010) 1470–1471.
[13] E. Hemmer, A. Benayas, F. Legare, F. Vetrone, Exploiting the biological windows: current perspectives on fluorescent bioprobes emitting above 1000 nm, Nanoscale Horiz. 1 (2016) 168–184.
[14] Z. Liao, H. Xu, W. Zhao, H. Yang, J. Zhong, H. Zhang, Z. Nie, Z.-K. Zhou, Energy transfer from Mn^{4+} to Mn^{5+} and near infrared emission with wide excitation band in $Ca_{14}Zn_6Ga_{10}O_{35}$:Mn phosphors, Chem. Eng. J. 395 (2020).
[15] R. Cao, X. Yu, X. Sun, C. Cao, J. Qiu, Near-infrared emission $Ba_3(PO_4)_2$:Mn^{5+} phosphor and potential application in vivo fluorescence imaging, Spectrochim. Acta A Mol. Biomol. Spectrosc. 128 (2014) 671–673.
[16] X. Zhang, J. Nie, S. Liu, J. Qiu, Structural variation and near infrared luminescence in Mn^{5+}-doped M_2SiO_4 (M = Ba, Sr, ca) phosphors by cation substitution, J. Mater. Sci. Mater. Electron. 29 (2018) 6419–6427.
[17] E.A. Medina, J. Li, J.K. Stalick, M.A. Subramanian, Intense turquoise colors of apatite-type compounds with Mn^{5+} in tetrahedral coordination, Solid State Sci. 52 (2016) 97–105.
[18] Y. Wang, H. Lei, P. Jiang, L. Liu, K. Cui, W. Cao, Synthesis and optical properties of intense blue colors oxides based on Mn^{5+} in tetrahedral sites in $Ba_7Al_{2-x}Mn_xO_{10+y}$, Ceram. Int. 47 (2021) 686–691.
[19] Y. Wang, H. Lei, P. Jiang, K. Cui, L. Liu, B. Li, W. Cao, Synthesis and optical properties of Mn-doped $Ba_3Al_2O_6$ intense blue oxides, Opt. Mater. 109 (2020).
[20] Y. Zhou, P. Jiang, H. Lei, Y. Li, W. Cao, J. Kuang, Synthesis and properties of novel turquoise-green pigments based on $BaAl_{2-x}Mn_xO_{4+y}$, Dyes Pigments 155 (2018) 212–217.
[21] Z. Wang, Y. Wang, M.A. Subramanian, P. Jiang, Structure and functional properties of oxides in the $BaO–Al_2O_3$ system: phosphors, pigments and catalysts, Prog. Solid State Chem. 68 (2022).
[22] B. Lazic, V. Kahlenberg, R. Kaindl, A. Kremenović, On the symmetry of $Ba_3Al_2O_6$ – X-ray diffraction and Raman spectroscopy studies, Solid State Sci. 11 (2009) 77–84.
[23] M.C. Biesinger, B.P. Payne, A.P. Grosvenor, L.W.M. Lau, A.R. Gerson, R.S.C. Smart, Resolving surface chemical states in XPS analysis of first row transition metals, oxides and hydroxides: Cr, Mn, Fe, Co and Ni, Appl. Surf. Sci. 257 (2011) 2717–2730.
[24] P. Jiang, T. Xiao, Y. Zhou, J. Kuang, Q. Wang, W. Cao, Facile synthesis of brownmillerite-type oxides $Ba_2In_{2-x}Mn_xO_{5+x}$ through a microwave-assisted process, Solid State Sci. 65 (2017) 1–5.
[25] S.W. Kim, G.E. Sim, J.Y. Ock, J.H. Son, T. Hasegawa, K. Toda, D.S. Bae, Discovery of novel inorganic Mn^{5+}-doped sky-blue pigments based on $Ca_6BaP_4O_{17}$: crystal structure, optical and color properties, and color durability, Dyes Pigments 139 (2017) 344–348.
[26] S. Li, J. Wu, R. Li, Z. Zhang, Z. Qiu, Y. Liu, S. Lian, Near-infrared emission of Cr^{3+} in five-coordinated field, Ceram. Int. 49 (2023) 14581–14586.
[27] X. Zhang, Y. Li, Z. Hu, Z. Chen, J. Qiu, A general strategy for controllable synthesis of $Ba_3(MO_4)_2$:Mn^{5+} (M = V, P) nanoparticles, RSC Adv. 7 (2017) 10564–10569.
[28] M.D. Dramicanin, L. Marciniak, S. Kuzman, W. Piotrowski, Z. Ristic, J. Perisa, I. Evans, J. Mitric, V. Dordevic, N. Romcevic, M.G. Brik, C.G. Ma, Mn(5+)-activated Ca(6)Ba(PO(4))(4)O near-infrared phosphor and its application in luminescence thermometry, Light Sci. Appl. 11 (2022) 279.
[29] Y. Ding, X. Zhang, H. Gao, S. Xu, C. Wei, Y. Zhao, Enhancement on concentration quenching threshold and upconversion luminescence of β-$NaYF_4$:Er^{3+}/Yb^{3+} codoping with Li^+ ions, J. Alloy. Compd. 599 (2014) 60–64.
[30] Z. Ristić, W. Piotrowski, M. Medić, J. Periša, Ž.M. Antić, L. Marciniak, M. D. Dramićanin, Near-infrared luminescent lifetime-based thermometry with Mn^{5+}-activated $Sr_3(PO_4)_2$ and $Ba_3(PO_4)_2$ phosphors, ACS Appl. Electron. Mater. 4 (2022) 1057–1062.
[31] X. Feng, L. Lin, R. Duan, J. Qiu, S. Zhou, Transition metal ion activated near-infrared luminescent materials, Prog. Mater. Sci. 129 (2022).
[32] W.M. Piotrowski, R. Marin, M. Szymczak, E. Martín Rodríguez, D.H. Ortgies, P. Rodríguez-Sevilla, M.D. Dramićanin, D. Jaque, L. Marciniak, Mn^{5+} lifetime-based thermal imaging in the optical transparency windows through skin-mimicking tissue phantom, Adv. Opt. Mater. 11 (2022).
[33] X. Yin, W. Xu, G. Zhu, Y. Ji, Q. Xiao, X. Dong, M. He, B. Cao, N. Zhou, X. Luo, L. Guo, B. Dong, Towards highly efficient NIR II response up-conversion phosphor enabled by long lifetimes of Er(3), Nat. Commun. 13 (2022) 6549.